# The kinetic of calcium silicate hydrate formation from silica and calcium hydroxide nanoparticles

Rachel Camerini [a,1], Giovanna Poggi [a,1], Francesca Ridi [a,*], Piero Baglioni [b,*]

[a] Department of Chemistry "Ugo Schiff" and CSGI, University of Florence, Via della Lastruccia 3, 50019 Sesto Fiorentino (FI), Italy
[b] CSGI, University of Florence, Via della Lastruccia 3, 50019 Sesto Fiorentino (FI), Italy

GRAPHICAL ABSTRACT
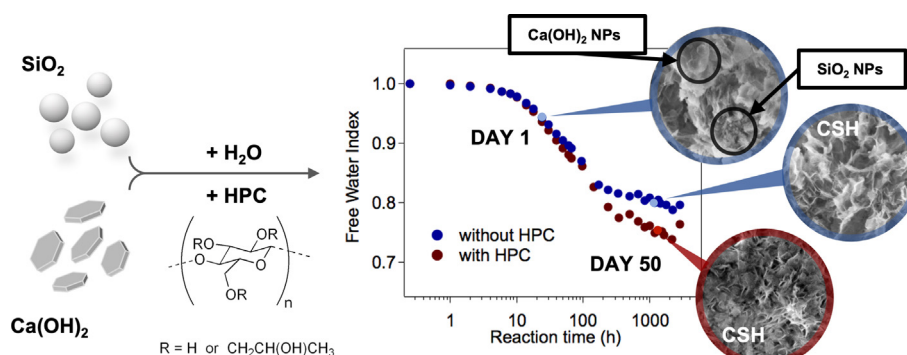
ARTICLE INFO

ABSTRACT

Hypothesis: The mechanism of calcium silicate hydrate (CSH) formation, a relevant component of cement, the largest used material by mankind, is well documented. However, the effects of nano-sized materials on the CSH formation have not yet been evaluated. To this aim, a kinetic study on CSH formation via the "pozzolanic reaction" of nanosilica and calcium hydroxide nanoparticles, and in the presence of hydroxypropyl cellulose (HPC) as hydration regulator, is reported in this paper.

Experiments: The reagents were mixed with water and cured at 10, 20, 30 and 40 °C. The reaction kinetics was studied with differential scanning calorimetry (DSC). A Boundary Nucleation and Growth model (BNGM) combined with a diffusion-limited model was used to analyze the data, yielding induction times, reaction rates, activation energies, nucleation and linear growth rates, and the related diffusion coefficients.

Findings: The rate constants k_B and k_G, which are, respectively, the rate at which the nucleated boundary area transforms, and the rate at which the non-nucleated grains between the boundaries transform, increase with temperature. Their different temperature dependence accounts for the prevailing effect of nucleation over nuclei growth at progressively lower temperatures. The nucleation rate, I_B, is strongly enhanced when using nanomaterials, while the linear growth rate, G, is limited by the tightly packed structure of the transforming matrix. HPC influences the kinetics between 10 and 30 °C; at 40 °C the temperature effect becomes predominant. HPC delays induction and acceleration periods, increases $E_a(k_B)$, and enhances the reaction efficiency during the diffusion regime, by retaining and delivering water over the matrix, thus allowing a higher water consumption in the hydration reaction of CSH.

© 2021 Elsevier Inc. All rights reserved.

---

* Corresponding authors.
  E-mail addresses: francesca.ridi@unifi.it (F. Ridi), baglioni@csgi.unifi.it (P. Baglioni).
[1] These authors contributed equally.

1. Introduction

Calcium silicate hydrates (CSH) include natural and synthetic phases, whose structure ranges from semi-crystalline to nearly amorphous, with variable stoichiometry [1,2]. The general formula $(CaO)_x \cdot SiO_2 \cdot (H_2O)_y$ implies large variability in CSH composition and properties. Synthetic CSH is commonly obtained from the hydration of calcium silicates in cement pastes, i.e. tricalcium silicate (C_3S) or β-dicalcium silicate (C_2S), and represents the main binding phase of cement-based materials, contributing to their mechanical properties and cohesion [2–6]. The Ca/Si ratio in cement pastes usually varies from 0.4 to 3, while the water/solid ratio ranges from 0.3 to 8 [7–10].

The use of fumed silica was found to accelerate the early hydration of cement and to increase the amount of CSH [11–13]. CSH can be also obtained from the reaction of Ca salts with alkali silicates or SiO_2, in the presence of water [2,14–18]. For instance, silica-lime reaction usually yields CSH with Ca/Si ratio of 1.5, while higher ratios can be obtained from C_3S [10,19].

Smaller silica particles, such as silica fume or silica nanoparticles, can be mixed at room temperature with calcium oxide or hydroxide to obtain CSH phases via the "pozzolanic reaction", i.e. the reaction of finely dispersed siliceous/aluminous materials with calcium hydroxide in the presence of water [7,20,21], to form compounds with cementitious properties [22]. Lin *et al.* studied Ca(OH)$_2$-activated nano-SiO_2 cements as bioactive cements for bone regeneration, and found shorter setting times and lower heat release than pure C_3S with the same reaction stoichiometry [23]. The process starts with the break of the siloxane bonds due to alkaline activation. Thereafter, Ca^{2+} ions offset the charge imbalance by bonding to silanol groups forming the CSH gel. The ability of such materials to set in humid and wet environments (water, saliva, blood and other fluids) makes them also useful for dental biomedical applications [24]. Recently, Daniele *et al.* investigated the interactions of silica fume with Ca(OH)$_2$ aqueous suspensions stabilized by a non-ionic surfactant, which leads to the formation of CSH phases with lower energy consumption and CO_2 emission with respect to traditional products, i.e. ordinary Portland cements [25].

The cementing properties of CSH have been also recently exploited in the field of cultural heritage conservation, where consolidation of carbonate-based materials, including *frescoes* and stones, can be achieved with alkaline earth metal hydroxides nanoparticles [26,27]. In a recent study, a system based on nanosilica and calcium hydroxide nanoparticles was developed for the consolidation of adobe, an earthen powdery substrate of archaeological and architectural interest [28]. Adobe bricks, obtained by mixing earth with water and drying the mixture under sunlight, are particularly susceptible to wind and water erosion, and degrade easily. The "in situ" formation of CSH phases within the porosities of the treated adobe material, due to the reaction of nanosilica with Ca(OH)$_2$ nanoparticles, granted the consolidation of the adobe bricks. Hydroxypropyl cellulose (HPC), included in the consolidating mixture, performed three main actions: it acts as a viscosity-modifier, provides flexural strength, and reduces hygrometric shrinkage during drying [28]. Following these results, we decided to study the kinetics of CSH formation starting from nanosized reactants, also in the presence of HPC. Several studies have been carried out on the mechanism of CSH formation over the years [6,11,24,29–33]. The most recent advancement in the field includes the quantitative monitoring of the hydration process in terms of transient local molecular composition using solid-state nuclear magnetic resonance [34] and the study of the distribution of hydration products in high spatial, temporal, and spectral resolution using Raman microspectroscopy [35]. However, to the best of our knowledge, this is the first kinetic study of the reaction of silica and calcium hydroxide nanoparticles. It is worth noting that, in modern cement chemistry, cellulose ethers (HCP) are commonly used to modify the rheology of the pastes. The presence of these organic polymers is reported to influence the initial phase of the hydration and its temperature dependence, without affecting the kinetic laws describing the process [32,33,36–39].

CSH formation over time was studied through a method based on Differential Scanning Calorimetry (DSC), which allows to monitor the hydration process of cement [6]. This approach quantifies the unreacted water at different hydration times through the integration of the melting peak measured by DSC, which allows to obtain the Free Water Index (FWI) [6,36,37]. Early stages of the kinetics were described by using the Boundary Nucleation and Growth Model (BNGM), originally proposed by Thomas for the study of the formation of CSH from pure C_3S [40], and recently used to study the carbonation kinetics of calcium hydroxide nanoparticles [41]. The BNGM is a geometry-controlled kinetic model that takes into account nucleation and growth processes occurring at the interface of reacting grains. In cement pastes, hydrate phases form first on the surface of the particles, then grow along the surface, eventually covering the reacting grains, and outward into the pore space, until the reacted regions coalesce, causing the paste to set. This model allows to separately evaluate the contribution of boundary CSH nucleation and growth, and accounts for the important effect of reactants' surface area on the reaction kinetics. Later stages of the CSH formation are here described by a diffusion-limited model.

The reaction rate constants were obtained at four different temperatures, with and without HPC, and the activation energy, the nucleation rate and the linear growth rate were calculated. Fourier Transform Infrared (FT-IR) Spectroscopy, Thermogravimetric Analysis (TGA) and Scanning Electron Microscopy (SEM) were also performed to gain information on the composition and morphology of the new forming phase.

2. Materials and methods

2.1. Materials

Metal granular calcium (Aldrich, 99%) and ethanol absolute (Sigma-Aldrich, 99.8%) were used for the synthesis of calcium hydroxide nanoparticles. Monodisperse spheres of amorphous SiO_2 (Levasil CS40-213 - Nouryon, 40 wt% in water, 0.2 wt% of Na_2O as stabilizer, pH = 9) were used. Hydroxypropyl cellulose (Klucel®-G - Phase Restauro, technical grade, MW: 370,000 Da, moles of substitutions: 2–4.1) was used as additive for the preparation of CSH samples. Water was purified by a Millipore Milli-Q UV system (resistivity > 18 MΩ·cm). KBr (FT-IR grade, Merck) for FT-IR analysis was used as received.

2.2. Samples' preparation

Calcium hydroxide nanoparticles in ethanol, with 100–200 nm diameter and a surface area of 36 m^2/g were prepared by a solvothermal synthesis [42,43]. Calcium hydroxide nanoparticles and silica nanoparticles were dried overnight at 130 °C, under N_2 flow. After drying, a small amount of calcium carbonate in the dried calcium hydroxide particles was assessed with TGA, to evaluate precisely the weight of reacting Ca in the powder. An aqueous solution of HPC was prepared at a concentration of 1 wt% by stirring the mixture overnight. Calcium silicate hydrate (CSH) was prepared by mixing the two powders with a reacting Ca/Si ratio of 0.9 by mass, and then adding the HPC solution or pure water (for samples with or without the cellulosic additive, respectively), to obtain

a paste with a 0.8 water/solid ratio by mass. Samples' pH is about 12, regardless of the composition. Eight samples were prepared, four without HPC and four with HPC. The former samples are labelled with the curing temperature (e.g. '10'), the latter ones with the curing temperature followed by '_HPC' (e.g. '10_HPC').

2.3. Methods

Differential scanning calorimetry (DSC) measurements were performed with a DSC-Q2000 from TA Instruments (New Castle, USA). About 40 mg of the paste was placed in a steel pan (diameter 7.4 mm, capacity 60 μl) and sealed with a cover equipped with a neoprene O-ring to avoid water evaporation and carbonation of calcium hydroxide nanoparticles. The remaining part of the paste was placed in a sealed Eppendorf tube. Each sample was maintained at constant temperature in a dry block heater (10 °C, 20 °C, 30 °C, or 40 °C) and DSC pans were periodically analyzed. The measurements were carried out with the following temperature program: isothermal for 4 min at −60 °C, ramp from −60 °C to +50 °C at 5 °C/min.

The melting enthalpy of water was obtained from the endothermic peak between −35 and +20 °C. The area of the peak decreases over time, as unreacted water is gradually consumed by the reaction. The time evolution of the melting peak is reported in Fig. 1.

The melting enthalpy of water was used to calculate the Free Water Index (FWI) according to the formula [6,36]:

$$FWI = \frac{\Delta H_{exp}}{\Phi_w \Delta H_{theor}} \tag{1}$$

where ΔH_{exp} is the experimental melting enthalpy, Φ_w is the original weight fraction of water in the sample, and ΔH_{theor} is the theoretical value of the melting enthalpy of water (333.4 J/g). Changes in FWI were plotted against reaction time and the curves were fitted using the boundary nucleation and growth model (BNGM) for early stages, combined with a diffusion-limited model for the later stages of the reaction.

BNGM was originally developed by Cahn for metal phases transformations [44] and later used by Thomas to describe the hydration of tricalcium silicate grains [40]. A detailed treatment of the geometrical derivation of this model can be found elsewhere [32,40,44–48]. Here only the basic concepts of the BNGM are reported. The derivation considers an untransformed volume containing a single planar boundary and assumes that the transformed phase only nucleates at spatially random locations on this boundary. Then, a single growing spherical region of nucleated product which intersects a plane parallel to the boundary (at a perpendicular distance y) is considered. The integration of the area fraction of intersection, over all values of the perpendicular distance y between the plane and the boundary, gives the volume fraction of transformed phase originating from nuclei on the same grain boundary, X, which can be expressed as follows:

$$X = 1 - exp[-2O_V^B \int_0^{Gt} (1 - exp(-Y^e))dy] \tag{2}$$

where O_V^B is the total area of the grain boundaries (randomly distributed in the original untransformed volume) per unit volume, G is the linear growth rate, t is the time since the start of the transformation, y is the perpendicular distance of a plane parallel to the boundary from the transforming boundary (i.e., Gt), Y^e is the extended area fraction of the intersection between the plane at distance y from the boundary and all regions nucleated on the grain boundary. Y^e can be mathematically described as:

$$Y^e = \frac{\pi I_B}{3} G^2 t^3 \left[1 - \frac{3y^2}{G^2 t^2} + \frac{2y^3}{G^3 t^3}\right] \quad if \quad t > y/G \quad Y^e = 0 \quad if \quad t < y/G \tag{3}$$
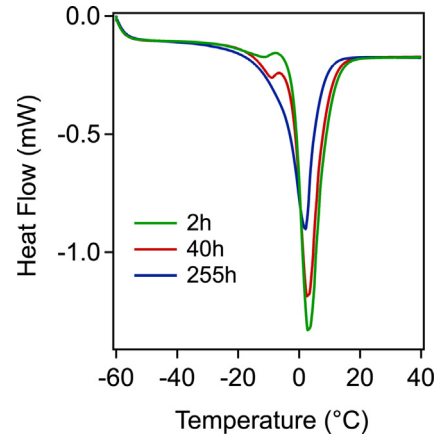

Fig. 1. Heat flow of '10_HPC' sample at different reaction times.

where I_B is the nucleation rate per unit area of untransformed boundary.

The volume of the transformed phase depends on three covariant parameters (G, I_B, and O_V^B) such that Eq. (2) has only two degrees of freedom, identified by Thomas as two independent rate constants, named k_B and k_G. They are defined respectively as the rate at which the nucleated boundary area transforms, and the rate at which the non-nucleated grains between the boundaries transform (i.e. the rate at which the porosities are filled with reaction products) [40]. The linear growth rate, G, and the nucleation rate, I_B, are obtained from k_B and k_G by the following relationships:

$$k_B = (I_B O_V^B)^{1/4} G^{3/4} \tag{4}$$

$$k_G = O_V^B G \tag{5}$$

Eq. (3) can be transformed by performing a change of variable from $y = Gt$ to $z = y/G$, [40]:

$$Y^e = \frac{\pi}{3} \frac{k_B^4}{k_G} t^3 \left[1 - \frac{3z^2}{t^2} + \frac{2z^3}{t^3}\right] \quad if \quad t > z \tag{6}$$

and Eq. (2) becomes:

$$X = 1 - exp[-2k_G \int_0^t (1 - exp(-Y^e))dz] \tag{7}$$

Equations (6) and (7) can now be solved, and the parameters k_B and k_G can be directly accessed. In fact, by introducing FWI into Eq. (7) [5], FWI curves versus time can be fitted using the BNGM:

$$FWI(t < t_d) = FWI_d + (1 - FWI_d)exp\left[-2k_G \int_0^t (1 - exp(-Y^e))dz\right] \tag{8}$$

where FWI_d is the fraction of unreacted water still present at the beginning of the diffusion period, which starts at time t_d.

Fitting the time evolution of FWI using Eq. (6) and Eq. (8) returns the independent parameters k_B, k_G and FWI_d. The values of the linear growth rate, G, and of the nucleation rate, I_B, can be then calculated through Eq. (4) and Eq. (5), using k_B, k_G, and O_V^B. The value of O_V^B in our system is 151 μm^{-1} and was obtained dividing the surface area of the dry silica nanoparticles powder (100 m²/g) by the volume occupied by the products after complete reaction (0.662 cm³/g), as reported elsewhere [40].

It is important to note that the BNG model is only valid for t < t$_d$. For t > t$_d$, the well-known diffusion-limited model is used to describe the reaction kinetics. The rate-limiting process at later stages of the reaction is the diffusion of the water through the layer

of CSH surrounding the unreacted particles. Therefore, when t > t$_d$, the equation that describes the time evolution of FWI is:

$$FWI(t > t_d) = \left\{ FWI_d^{1/3} - \frac{(2D)^2}{\langle R \rangle}(t - t_d)^{1/2} \right\}^3 \qquad (9)$$

where D is the diffusion constant, and $\langle R \rangle$ is the average size of the calcium hydroxide nanoparticles.

In this regime, the reaction rate depends on the ability of water to diffuse through calcium hydroxide nanoparticles, whose dissolution triggers the process, i.e. the break of the siloxane groups of silica nanoparticles in alkaline environment, and the subsequent bonding with Ca^{2+} ions to form CSH [24].

BNGM equations combined with the diffusion-limited model have been therefore implemented and numerically solved using the software Igor Pro, version 6.2 (Wavemetrics Inc.).

SEM analyses were performed on samples in 1–50 days window from their preparation, to gather information on the morphology of the new forming phase. To this purpose, each sample was removed from the sealed Eppendorf tube and lyophilized prior to deposition on the stub, with the aim of hampering further hydration of the paste. For the observations, a field emission gun scanning electron microscope (FEG-SEM), ΣIGMA (Carl Zeiss, Germany), was used, with an acceleration potential of 2 kV and a working distance of ∼ 2 mm.

Fourier Transform Infrared (FT-IR) Spectroscopy and Thermogravimetric Analysis (TGA) were employed to get further insights on the formation of CSH: FT-IR was performed after 1 day and 50 days from samples' preparation, on the same lyophilized specimens used for SEM analyses. The analysis was performed using KBr pellets prepared with 1% of the collected samples, using a BIO-RAD FTS-40 spectrometer (Hercules, USA) with the following parameters: transmission mode, 4000–400 cm^{-1}, 64 scans, delay time of 300 s. The spectral data were elaborated using the Win-Ir software. TGA was carried out (on the same powders) using an SDT Q600 TA Instrument (New Castle, USA), operating between 25 and 800 °C, at a heating rate of 10 °C/min, under nitrogen flow (100 mL/min). For each measurement, about 5 mg of sample was placed inside an alumina pan.

The specific surface area of nanosilica and calcium hydroxide nanoparticles was determined by Brunauer-Emmett-Teller (BET) analysis of N_2 isotherms, obtained with a Coulter SA 3100 Surface area analyzer (Brea, USA), with an experimental error of about 5%. From the specific surface area, the average size of nanosilica was estimated by calculating the equivalent spherical diameter, or BET particle diameter (d$_{BET}$), from the equation: d$_{BET}$ = 6/(q*S$_w$), where q is the density of silica (2.65 g/cm^3) and S_w is the specific surface area [49]. The calculated d$_{BET}$ of nanosilica is 23 nm, which is in good accordance with the values reported in the literature, obtained from dynamic light scattering measurements [50]. Therefore, silica particles are 5–10 times smaller than calcium hydroxide nanoparticles.

3. Results and discussion

3.1. FT-IR spectroscopy and thermogravimetric analysis

FT-IR spectroscopy was performed on samples after 1 day and 50 days from their preparation. Fig. 2 shows a comparison between samples cured at 20 °C, without and with HPC.

In the FT-IR spectra of all the prepared samples, the characteristic signals of silicon-based compounds are present: in particular, the bands located at about 1100 cm^{-1} and 800 cm^{-1} are due to the internal Si-O-Si asymmetric and symmetric stretching, respectively; the band at 950 cm^{-1} is related to the Si-O stretching of surface Si-OH groups, and the band at 450 cm^{-1} is ascribed to the Si-
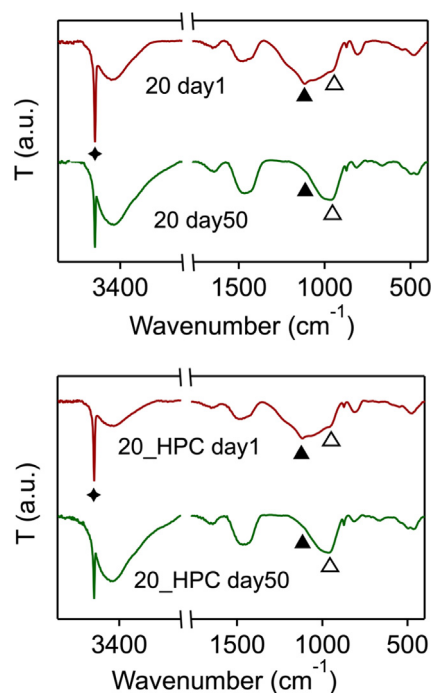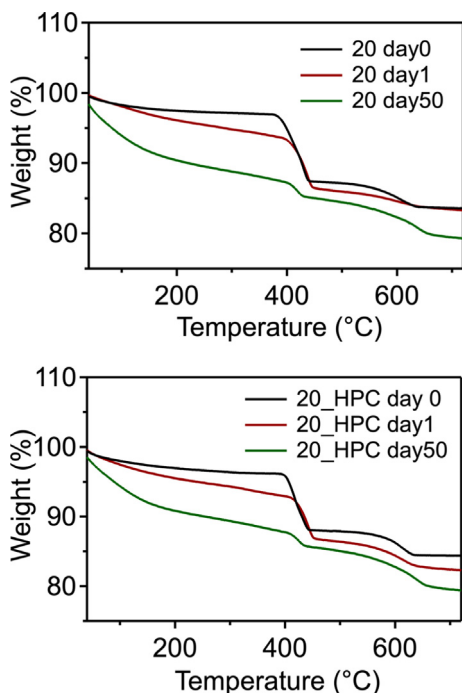

Fig. 2. FT-IR spectra collected after 1 day (red line) and 50 days (green line) on sample '20' (upper panel) and sample '20_HPC' (lower panel). Markers refer to calcium hydroxide (filled star), siloxane groups (filled triangles) and silanols (empty triangles), respectively. (For interpretation of the references to colour in this figure legend, the reader is referred to the web version of this article.)

O-Si asymmetric bending. It is interesting to note that, after 50 days, an inversion in the intensity of signals located at about 1100 cm^{-1} (filled triangle in Fig. 2) and 950 cm^{-1} (empty triangle) occurs. This phenomenon is due to the transformation of the siloxane groups in silanols, i.e silica depolymerization, and is a fingerprint of CSH formation [8,23,24,51]. In fact, the process starts with the dissolution of $Ca(OH)_2$ in water, followed by the break of the Si-O-Si covalent bonds by the released OH groups; afterwards, Ca^{2+} ions bridge to the depolymerized silica and form the basic unit of CSH [24].

The narrow peak centered at 3650 cm^{-1} (filled star in Fig. 2), due to $Ca(OH)_2$ [52], shows a decrease after 50 days of curing at 20 °C, confirming the consumption of the reactant due to the formation of CSH. The band at 1350–1550 cm^{-1} (asymmetric CO_3 stretching, ν_3), the peak at 876 cm^{-1} (asymmetric CO_3 bending, ν_2), and the peak at 713 cm^{-1} (symmetric CO_3 bending, ν_4 (calcite)) are due to the presence of small amount of calcium carbonate [53–55] in the dried nanoparticles, which was formed prior to the preparation of the pastes (see section 2.2) and did not affect the hydration reaction.

The broad band centered at 3400 cm^{-1} and the small band at 1650 cm^{-1}, related to OH stretching and bending, can be ascribed to water, residual OH groups of silica, and HPC, when present.

Interestingly, the thermogravimetric analyses performed on the same samples (Fig. 3) show that the formation of CSH has already started after 24 h from the samples preparation, as shown by the mass loss up to 380 °C, which is due to the decomposition of hydrate phases [37,56,57]. It is worth noting that the amount of CSH is significantly higher after 50 days from samples' preparation. The well-defined mass loss between 400 and 450 °C can be ascribed to calcium hydroxide, which is not completely consumed after 50 days of curing, as also shown by the FTIR analysis. The presence of HPC seems to produce a slight increase on the decomposition temperature of both the aforementioned phases, without influencing the chemical nature of the newly formed phases [37].

Fig. 3. TGA curves collected on pastes before curing (black line), and after 1 day (red line) and 50 days (green line) on sample '20' (upper panel) and sample '20_HPC' (lower panel). (For interpretation of the references to colour in this figure legend, the reader is referred to the web version of this article.)

3.2. Differential scanning calorimetry

Experimental data obtained from FT-IR and TGA measurements clearly show the formation of CSH starting from nanosilica and calcium hydroxide nanoparticles in the selected curing condition. The kinetics of this process was therefore studied with DSC. The FWI values of the samples were plotted against the reaction time, and the data were fitted by combining the BNGM (8) and the diffusion-limited model (9). The obtained parameters are reported in Table 1. Fig. 4 shows the best results for the samples at four temperatures (10 °C, 20 °C, 30 °C, and 40 °C), without and with HPC (blue and red markers, respectively). All the curves are characterized by an induction period, where FWI is almost constant, and an acceleration period, where water consumption increases. The induction time, t_i, is obtained as the intersection of the lines describing the induction and the acceleration periods. The nucleation and growth phase ends when t_d is reached; after that, the process slows down, and the diffusion regime becomes predominant.

For all samples, the induction period is reduced from 10 h (samples cured at 10 °C) to less than 4 h (samples cured at 40 °C). The acceleration period is also reduced with increasing temperature, i.e., from 3 to 4 weeks for samples cured at 10 °C to 2–3 days for those cured at 40 °C.

The presence of HPC delays the start of the acceleration period only at 10 °C, where t_i is 1.5–2 times higher than that of the same system without the cellulosic additive.

The acceleration period is extended by the presence of HPC, with exception of the highest temperature considered (40 °C), where this effect is negligible. These findings are in agreement with literature data about the hydration kinetics of C_3S, where the presence of additives generally increases the duration of the induction and acceleration steps [37,39,58].
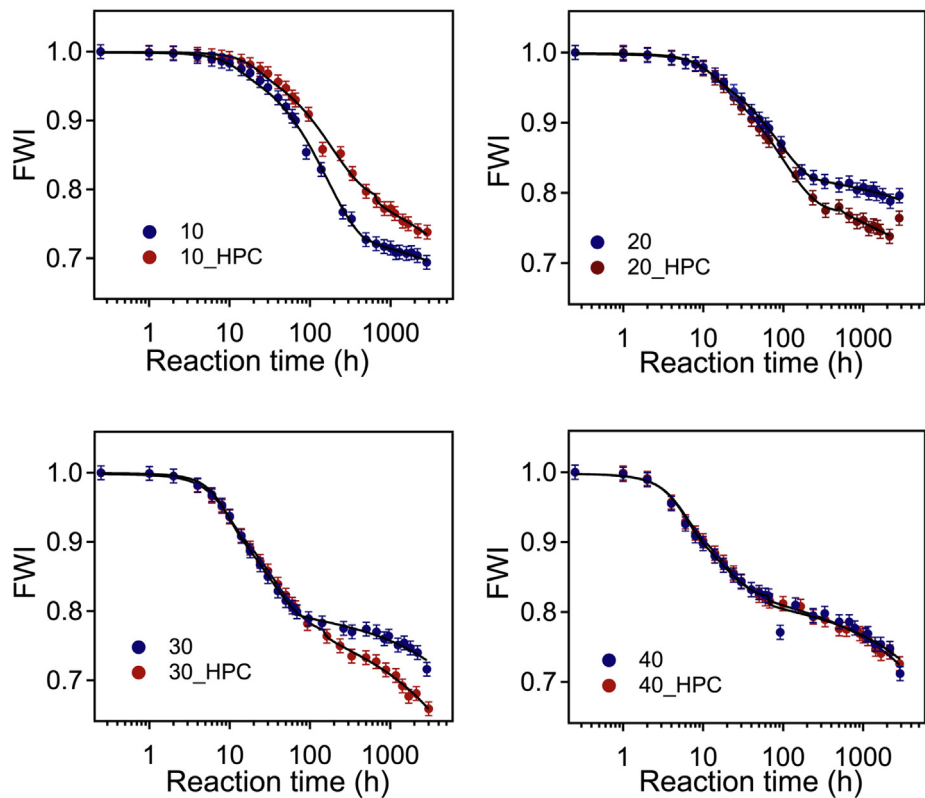
3.2.1. BNGM – k_B, k_G, and activation energies

The BNG model returned the rate constants k_B, the rate at which the nucleated boundary area transforms, and k_G, the rate at which the non-nucleated grains between the boundaries transform (i.e., the rate at which the porosities are filled with reaction products).

Regardless of the system composition, k_B and k_G increase with increasing temperature, while the presence of HPC leads to a decrease of both rate constants for all the curing temperatures investigated (see Table 1).

Two limiting cases can be described by the k_B/k_G ratio [40]: for $k_B/k_G \gg 1$, the boundary region is densely populated with nuclei that completely react in the process. On the contrary, when $k_B/k_G \ll 1$, the internal boundaries are sparsely populated with nuclei and transform at the same rate as the whole system. The latter case approaches a 'spatially random nucleation', which can be well described with the standard Avrami equation [59].

In our case, at 40 °C, neither nucleation nor growth is the dominant contribution to the process; at progressively lower temperatures the k_B/k_G ratio increases: in fact, both k_B and k_G rate constants decrease, but it is worth noting that the decrease of k_G, which is almost halved with every curing temperature step, is significantly faster than the decrease of k_B. In other terms, with decreasing temperature, a progressive increase in the contribution of nucleation, which is mainly described by the k_B term, takes place. This is clearly shown by the Arrhenius plot, $\ln(k)$ versus $1/T$, which describes the temperature dependence of the two rate constants (Fig. 5).

In Fig. 5, the blue markers are used for systems without HPC, while the red markers are used for systems containing the cellulosic additive. All the Arrhenius plots are linear across the investigated temperature range, with a $R^2 \geq 0.97$, as indicated in Table 2. The higher dependence on temperature of k_G with respect to k_B, shown by the Arrhenius plots, is confirmed by the calculated activation energies (E_a) reported in Table 2.

Table 1
Fitting parameters obtained by combining the BNGM and the diffusion-limited models. The standard deviations in least significant digits are reported between brackets.

Sample name	t_i (h)*	t_d (h)	FWI_d	k_B (h^{-1})	k_G (h^{-1})	k_B/k_G	D (10^{-21} m^2 h^{-1})
10	10(1)	542(3)	0.73(1)	0.033(3)	0.0061(5)	5.41	0.4(3)
10_HPC	18(1)	646(3)	0.79(1)	0.022(2)	0.0053(6)	4.15	1.1(5)
20	8(1)	245(3)	0.82(1)	0.041(2)	0.012(1)	3.42	0.3(2)
20_HPC	8(1)	497(3)	0.78(1)	0.032(2)	0.010(1)	3.20	0.9(5)
30	4(1)	69(2)	0.80(1)	0.072(3)	0.033(2)	2.18	1.3(4)
30_HPC	4(1)	150(3)	0.77(1)	0.067(3)	0.028(3)	2.39	3.9(8)
40	< 4	66(2)	0.81(1)	0.110(3)	0.067(7)	1.64	1.8(5)
40_HPC	< 4	64(2)	0.82(1)	0.106(5)	0.057(6)	1.86	2.6(5)

*the induction time t_i is obtained as the junction point of the lines describing the induction and the acceleration periods.

Fig. 4. Kinetics of CSH formation from $Ca(OH)_2$ nanoparticles and SiO_2 nanoparticles without HPC (blue markers) and with HPC (red markers). The BNGM fittings combined with diffusion-limited model are reported on each data set as continuous black lines. (For interpretation of the references to colour in this figure legend, the reader is referred to the web version of this article.)
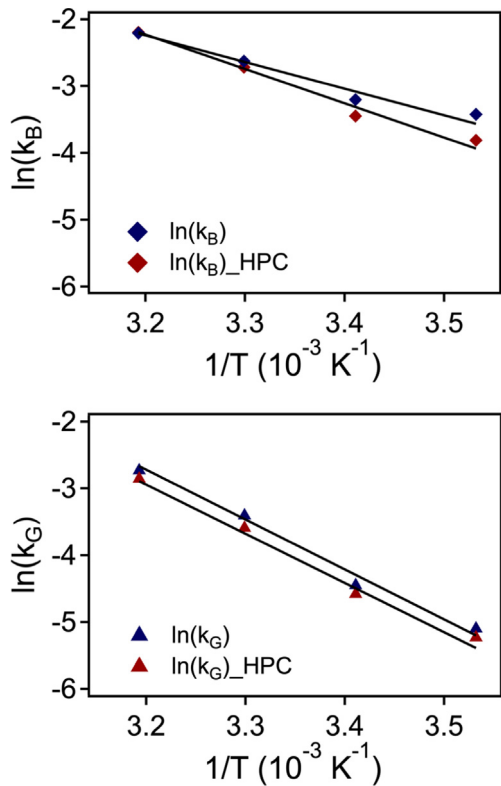
Fig. 5. Arrhenius plot showing the temperature dependence of the rate constants, k_B (upper panel) and k_G (lower panel), without HPC (blue markers) and with HPC (red markers). The experimental data were fitted with linear regressions (black lines). (For interpretation of the references to colour in this figure legend, the reader is referred to the web version of this article.)

Table 2
R^2 of the Arrhenius plots and activation energies calculated for k_B and k_G.

	R^2 (k_B)	R^2 (k_G)	E_a (k_B) (kJ/mol)	E_a (k_G) (kJ/mol)
without HPC	0.97	0.99	31(4)	60(4)
with HPC	0.98	0.99	41(4)	60(4)

The lower temperature dependence of k_B can be explained by taking into account the high surface area of reacting nanoparticles: in fact, the high extension of boundaries available for nucleation probably makes the effect of curing conditions, i.e., temperature, less relevant in the initial phase of the reaction.

Interestingly, HPC increases the temperature dependence of k_B, as shown by the increase in E_a (k_B). This might be explained by the absorption of the cellulosic additive on the reacting nanoparticles' surface, which decreased the amount of available boundary area that results in a significantly increased effect of the environmental conditions on the rate at which the nucleated boundary area transforms.

On the contrary, HPC does not affect E_a (k_G). In other terms, the presence of the cellulosic additive seems not to influence the rate at which the porosities are filled with reaction products, which is mainly described by the k_G term.

3.2.2. BNGM – I_B and G

Table 3 shows the values of I_B (nucleation rate) and G (linear growth rate) for each sample, calculated from k_B and k_G, using equations (4) and (5), in which the total area of the grain boundaries per unit volume, O_V^B, is introduced.

Table 3
Nucleation rate, I_B, and linear growth rate, G, obtained from the BNG model.

Sample name	I_B ($\mu m^{-2} \cdot h^{-1}$)	G ($\mu m \cdot h^{-1}$)
10	$11(6) \cdot 10^4$	$40(3) \cdot 10^{-6}$
10_HPC	$35(27) \cdot 10^3$	$35(4) \cdot 10^{-6}$
20	$39(21) \cdot 10^3$	$77(8) \cdot 10^{-6}$
20_HPC	$22(10) \cdot 10^3$	$68(8) \cdot 10^{-6}$
30	$17(6) \cdot 10^3$	$22(1) \cdot 10^{-5}$
30_HPC	$21(11) \cdot 10^3$	$18(2) \cdot 10^{-5}$
40	$12(5) \cdot 10^3$	$43(5) \cdot 10^{-5}$
40_HPC	$18(9) \cdot 10^3$	$38(4) \cdot 10^{-5}$

The trend of G reflects that of k_G, i.e., it increases with increasing temperature and is reduced by the presence of HPC regardless of the temperature. On the contrary, I_B decreases with increasing temperatures.

It is interesting to note that the I_B values of our systems are orders of magnitude higher than those reported in the literature for CSH formation in cement pastes, which generally range from 10^{-4} to 10 [32,39,40,58]. This is due to the fact that both silica and calcium hydroxide nanoparticles' have a high surface area, respectively of 100 m^2/g and 36 m^2/g, which result in an impressive increase in the number of nuclei in the system. A scheme of the time evolution of the formation of CSH due to the reaction of silica and calcium hydroxide nanoparticles is shown in Fig. 6.

On the contrary, the linear growth rates obtained for our systems are significantly lower than those reported in literature for CSH formation in cement [32,39,40,58]. Again, this might be

explained by the nanosized particles used as reactants, which probably arrange in a packed structure that limits the outward growth into the pore space, resulting in low G values.

Overall, the results obtained using the BNGM point out the combined effect of nanoparticles, curing conditions and HPC on the kinetics of CSH formation from nanosilica and calcium hydroxide nanoparticles. To summarize, HPC extends the induction period, at 10 °C, and the acceleration period, between 10 and 30 °C. At 40 °C, temperature seems to be the leading factor and the effect of the additive appears negligible. This might be explained by the fact that at about 40 °C HPC displays a cloud point [60], which leads to the precipitation of the polymer that is not anymore available to interact with the reactants. HPC has also a major influence on the early stages of the reaction, as it probably reduces the available surface area of reacting nanoparticles, and hence modifies the temperature dependence of the rate constant k_B. The obtained nucleation rates, which are significantly higher than those measured on cement pastes, can be ascribed to the nanosized materials, whose high surface area favors CSH formation. On the contrary, low linear growth rate are due to a tightly packed structure created by nanoparticles in which the growth of nucleated material in the pore space is partially hampered.

3.2.3. Diffusion period

The beginning of the diffusion period is delayed by the decrease in curing temperature and by the presence of HPC. The diffusion coefficient, D, (last column of Table 1), obtained from fitting the
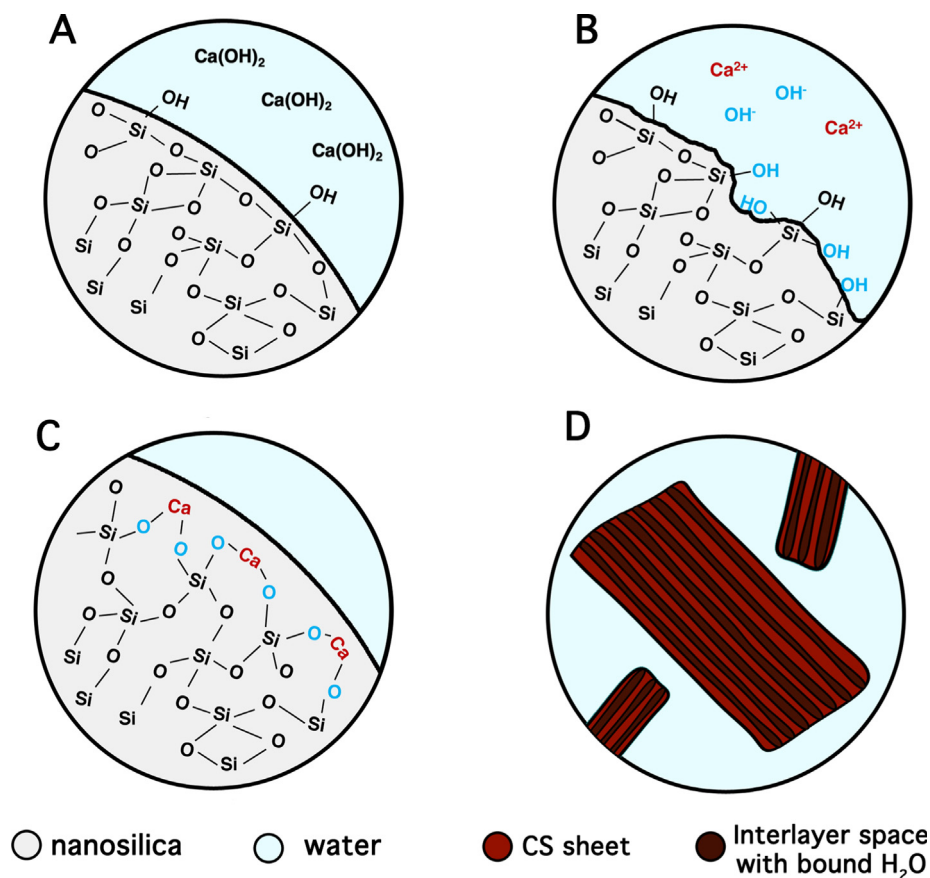
Fig. 6. Time evolution of CSH formation. Panel A shows a portion of a grain of nanosilica immersed in the reaction media, together with alkaline nanoparticles. The reaction starts with the dissolution of Ca(OH)$_2$ in water followed by a depolymerization of silica, to form silanol groups (panel B). Afterwards, Ca^{2+} ions bridge to the depolymerized silica and form the basic unit of CSH (panel C). The use of nanosilica, whose surface area is 100 m^2/g, significantly increase the rate of the process. Panel D shows the system at the nanoscale: the primary units of CSH are polydisperse multilayer disks with calcium silicate (CS) sheets and interlayer space with bound water. These primary units organize themselves to form fractal structures below the micrometer length-scale, as reported in the literature [33].
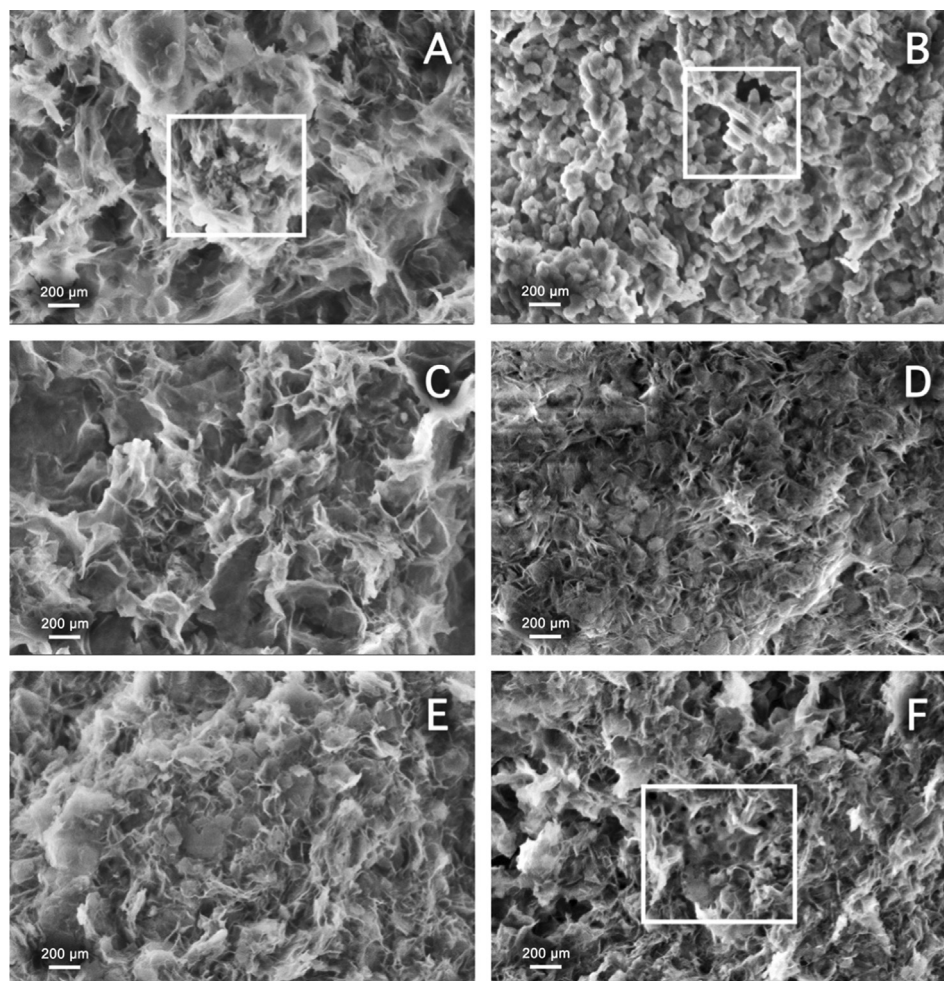
Fig. 7. SEM images (Mag = 100 kX) of (A) sample '20' after 1 day (WD = 2 mm), (B) sample '20_HPC' after 1 day (WD = 2 mm), (C) sample '20' after 50 days (WD = 2.9 mm), (D) sample '20_HPC' after 50 days (WD = 2.6 mm), (E) sample '30' after 50 days (WD = 2.6 mm), (F) sample '30_HPC' after 50 days (WD = 2.7 mm).

later stages of the kinetics, is related to the easiness for free water to reach the unreacted nanoparticles. As indicated above, CSH formation occurs through the break of the siloxane groups in alkaline environment, followed by the bridging of Ca^{2+} ions to the depolymerized silica [24]. Therefore, the diffusion regime starts when water needs to diffuse through the growing CSH matrix to reach unreacted hydroxide particles. Due to the fact that reactants must move through the nanopores within a continuous product layer around the unreacted particles [39,40], diffusion rates in cement are significantly smaller than those measured in bulk solutions. Moreover, the diffusion coefficients, obtained starting from nano-sized reactants, are smaller than those commonly obtained in standard cement pastes (10^{-21} vs 10^{-15} m^2/h). This is probably due to nanoparticles that create a denser-packed matrix with respect to micron-sized grains included in standard pastes, leading to a less porous structure, in which the diffusion of water is very low. Finally, it is worth noting that D values tend to increase with increasing temperature, which can be explained by the increased mobility of water in such environmental conditions.

Interestingly, the presence of HPC leads to the same overall effect, significantly increasing the D values up to a curing temperature of 30 °C. In cement chemistry, cellulosic additives act as regulators of water release, due to their carrying capacity and hydrophilicity, and water results homogeneously distributed and more prone to react [37,39,58,61]. Here a similar effect took place: the presence of HPC leads to a more efficient diffusion of water in the transforming gel matrix, resulting in a higher water consump-

tion in the later stages of the reaction, which starts from t_d. It is worth noting that at 40 °C, the presence of cellulose only slightly enhances the D parameter, probably because temperature becomes the driving force for the CSH formation as a result of the lower solubility of HPC at higher temperature.

3.3. Scanning Electron Microscopy

Fig. 7 reports SEM analysis after 1 day and 50 days from sample preparation. Fig. 7 A-D show samples cured at 20 °C, without cellulose (Fig. 7A and 7C, after 1 day and 50 days, respectively) and with cellulose (Fig. 7B and 7D, after 1 day and 50 days, respectively), while Fig. 7E and 7F show the samples cured at 30 °C, without and with cellulose, respectively.

After 1 day (acceleration phase), unreacted nanoparticles are still present, as shown in Fig. 7A (see the white box highlighting a group of SiO_2 spheres) and Fig. 7B (see the white box highlighting stacked platelets of $Ca(OH)_2$). After 50 days, CSH is the dominant phase, with the typical morphology of crumpled foils that characterizes alkaline activated silica [9,23]. In the presence of HPC (Fig. 7D), the classical CSH porous network displayed in Fig. 7C is partially covered up, due to the new forming phase embedded in the cellulosic matrix. At this stage, unreacted nanoparticles of silica and calcium hydroxide are still present, in agreement with the fact that the reaction is in the diffusion regime and that the FWI is still decreasing (see Fig. 4).

A similar effect is visible in samples cured at 30 °C, after 50 days (Fig. 7E and 7F). Interestingly, the footprint left by the reacted silica spheres in the matrix is clearly shown in Fig. 7F, as highlighted by a white box in the center of the image.

4. Conclusions

CSH was obtained starting from nanosilica and calcium hydroxide nanoparticles, and in the presence of hydroxypropyl cellulose, at different curing temperature. FT-IR and TGA measurements confirmed the formation of CSH, which has the typical morphology of crumpled foils that characterizes alkaline activated silica, as shown by SEM pictures. The reaction kinetics of CSH formation was studied by means of DSC, applying the BNGM combined with a diffusion-limited model.

The rate constants k_B and k_G, obtained from the BNGM, increase with temperature up to 40 °C when none of the two contributions is predominant. The contribution of nucleation prevails with decreasing temperature, according to the higher dependence on temperature of k_G with respect to k_B. The lower temperature dependence of k_B can be explained by taking into account the high surface area of reacting nanoparticles: in fact, the high extension of boundaries available for nucleation probably makes the effect of curing conditions, i.e., temperature, less relevant in the initial phase of the reaction.

The addition of a cellulosic additive delays the induction and acceleration periods, especially at low temperatures [37,39,58]. The presence of HPC decreases the rate at which the nucleated boundary area transforms (k_B), since it reduces the available surface area of the transforming nanoparticles. On the contrary, the rate at which the porosities are filled with the reaction products (k_G) is not significantly affected by the presence of the additive. Overall, HPC increases the temperature dependence of k_B (E_a = 41 ± 4 kJ/mol), but has no impact on k_G.

The use of nanosized reagents significantly influences the reaction kinetics in terms of I_B and G with respect to standard cement pastes [32,39,40,58]. In fact, I_B values are several orders of magnitude higher than those reported in the literature. This effect can be explained by taking into account the higher reactivity of nanomaterials, which enhances the nucleation rate. On the contrary, nanoparticles generate a packed structure limiting the outward growth of the reacting species into the pore space between the particles, because of steric hindrance, accounting for smaller G values in the BNGM kinetic model.

During the diffusion regime, which starts at t_d, the presence of HPC increases the water consumption, specially between 10 and 30 °C. This is due to the fact that HPC is able to retain water and distribute it in a controlled way water over the whole matrix, as reported for cement pastes [37,39,58,61]. At 40 °C the effect is no longer detectable, probably due to the precipitation of HCP aggregates, which makes temperature the driving force for CSH formation, regardless of the composition of the system. Overall, the addition of silica nanoparticle to calcium hydroxide nanoparticles consistently improves, as compared to the classic CSH occurring in the micrometer size cement powders, the nucleation process allowing for the control and the tuning of CSH formation.

In modern cement chemistry, the reaction of magnesium oxides with silica and water is exploited to produce an environmentally convenient alternative to standard binders based on CSH [62,63]. Future developments of our research foresee the study of the kinetic of magnesium silicate hydrate (MSH) formation in the presence of several additives, including cellulose derivatives and phosphates.

CRediT authorship contribution statement

Rachel Camerini: Investigation, Data curation, Formal analysis, Methodology, Writing - original draft, Writing - rewiew & editing. **Giovanna Poggi:** Investigation, Data curation, Formal analysis, Methodology, Visualization, Writing - original draft, Writing - rewiew & editing. **Francesca Ridi:** Conceptualization, Formal analysis, Methodology, Supervision, Validation, Writing - review & editing. **Piero Baglioni:** Conceptualization, Funding acquisition, Project administration, Resources, Supervision, Writing - review & editing.

Declaration of Competing Interest

The authors declare that they have no known competing financial interests or personal relationships that could have appeared to influence the work reported in this paper.

References

[1] S. Shaw, C. Henderson, B. Komanschek, Dehydrationr/recrystallization mechanisms, energetics, and kinetics of hydrated calcium silicate minerals: an in situ TGA/DSC and synchrotron radiation SAXS/WAXS study, Chem. Geol. 167 (2000) 141–159.

[2] J.J. Chen, J.J. Thomas, H.F.W. Taylor, H.M. Jennings, Solubility and structure of calcium silicate hydrate, Cem. Concr. Res. 34 (2004) 1499–1519, https://doi.org/10.1016/j.cemconres.2004.04.034.

[3] E. Gallucci, X. Zhang, K.L. Scrivener, Effect of temperature on the microstructure of calcium silicate hydrate (C-S-H), Cem. Concr. Res. 53 (2013) 185–195, https://doi.org/10.1016/j.cemconres.2013.06.008.

[4] S. Goñi, F. Puertas, M.S. Hernández, M. Palacios, A. Guerrero, J.S. Dolado, B. Zanga, F. Baroni, Quantitative study of hydration of C3S and C2S by thermal analysis, J. Therm. Anal. Calorim. 102 (2010) 965–973, https://doi.org/10.1007/s10973-010-0816-7.

[5] F. Ridi, E. Fratini, P. Baglioni, Cement: A two thousand year old nano-colloid, J. Colloid Interface Sci. 357 (2011) 255–264, https://doi.org/10.1016/j.jcis.2011.02.026.

[6] A. Damasceni, L. Dei, E. Fratini, F. Ridi, S.H. Chen, P. Baglioni, A novel approach based on differential scanning calorimetry applied to the study of tricalcium silicate hydration kinetics, J. Phys. Chem. B. 106 (2002) 11572–11578, https://doi.org/10.1021/jp020211l.

[7] R. Maddalena, K. Li, P.A. Chater, S. Michalik, A. Hamilton, Direct synthesis of a solid calcium-silicate-hydrate (C-S-H), Constr. Build. Mater. 223 (2019) 554–565, https://doi.org/10.1016/j.conbuildmat.2019.06.024.

[8] S. Grangeon, F. Claret, C. Roosz, T. Sato, S. Gaboreau, Y. Linard, Structure of nanocrystalline calcium silicate hydrates: Insights from X-ray diffraction, synchrotron X-ray absorption and nuclear magnetic resonance, J. Appl. Crystallogr. 49 (2016) 771–783, https://doi.org/10.1107/S1600576716003885.

[9] E.T. Rodriguez, I.G. Richardson, L. Black, E. Boehm-Courjault, A. Nonat, J. Skibsted, Composition, silicate anion structure and morphology of calcium silicate hydrates (C-S-H) synthesised by silica-lime reaction and by controlled hydration of tricalcium silicate (C3S), Adv. Appl. Ceram. 114 (2015) 362–371, https://doi.org/10.1179/1743676115Y.0000000038.

[10] I.G. Richardson, Model structures for C-(A)-S-H(I), Acta Crystallogr, Sect. B Struct. Sci. Cryst. Eng. Mater. B 70 (2014) 903–923, https://doi.org/10.1107/S2052520614021982.

[11] Z.Q. Wu, J.F. Young, The hydration of tricalcium silicate in the presence of colloidal silica, J. Mater. Sci. 19 (1984) 3477–3486, https://doi.org/10.1007/BF02396922.

[12] Y. Wei, W. Yao, X. Xing, M. Wu, Quantitative evaluation of hydrated cement modified by silica fume using QXRD, 27Al MAS NMR, TG-DSC and selective dissolution techniques, Constr. Build. Mater. 36 (2012) 925–932, https://doi.org/10.1016/j.conbuildmat.2012.06.075.

[13] M. Oltulu, R. Şahin, Pore structure analysis of hardened cement mortars containing silica fume and different nano-powders, Constr. Build. Mater. 53 (2014) 658–664, https://doi.org/10.1016/j.conbuildmat.2013.11.105.

[14] K. Sasaki, T. Masuda, H. Ishida, T. Mitsuda, Synthesis of Calcium Silicate Hydrate with Ca/Si = 2 by Mechanochemical Treatment, J. Am. Ceram. Soc. 80 (1996) 472–476, https://doi.org/10.1111/j.1151-2916.1997.tb02853.x.

[15] X. Cong, R. James Kirkpatrick, 29Si MAS NMR study of the structure of calcium silicate hydrate, Adv. Cem. Based Mater. 3 (1996) 144–156, https://doi.org/10.1016/s1065-7355(96)90046-2.

[16] A.W. Harris, M.C. Manning, W.M. Tearle, C.J. Tweed, Testing of models of the dissolution of cements - Leaching of synthetic CSH gels, Cem. Concr. Res. 32 (2002) 731–746, https://doi.org/10.1016/S0008-8846(01)00748-7.

[17] V. Kanchanason, J. Plank, Role of pH on the structure, composition and morphology of C-S-H–PCE nanocomposites and their effect on early strength development of Portland cement, Cem. Concr. Res. 102 (2017) 90–98, https://doi.org/10.1016/j.cemconres.2017.09.002.

[18] S.A. Greenberg, Reaction between silica and calcium hydroxide solutions. Kinetics in the temperature range 30 to 85°, J. Phys. Chem. 65 (1961) 12–16, https://doi.org/10.1021/j100819a005.

[19] E. Tajuelo Rodriguez, I.G. Richardson, L. Black, E. Boehm-Courjault, A. Nonat, J. Skibsted, Composition, silicate anion structure and morphology of calcium silicate hydrates (C-S-H) synthesised by silica-lime reaction and by controlled hydration of tricalcium silicate (C₃S), Adv. Appl. Ceram. 114 (2015) 362–371, https://doi.org/10.1179/1743676115Y.0000000038.

[20] R. Maddalena, C. Hall, A. Hamilton, Effect of silica particle size on the formation of calcium silicate hydrate [C-S-H] using thermal analysis, Thermochim. Acta. 672 (2019) 142–149, https://doi.org/10.1016/j.tca.2018.09.003.

[21] K. Garbev, P. Stemmermann, L. Black, C. Breen, J. Yarwood, B. Gasharova, Structural features of C-S-H(I) and its carbonation in air-A Raman spectroscopic study. Part I: Fresh phases, J. Am. Ceram. Soc. 90 (2007) 900–907, https://doi.org/10.1111/j.1551-2916.2006.01428.x.

[22] D.R.G. Mitchell, I. Hinczak, R.A. Day, Interaction of silica fume with calcium hydroxide solutions and hydrated cement pastes, Cem. Concr. Res. 28 (1998) 1571–1584, https://doi.org/10.1016/S0008-8846(98)00133-1.

[23] Q. Lin, X. Lan, Y. Li, Y. Ni, C. Lu, Y. Chen, Z. Xu, Preparation and characterization of novel alkali-activated nano silica cements for biomedical application, J. Biomed. Mater. Res. - Part B Appl. Biomater. 95 B (2010) 347–356. Doi: 10.1002/jbm.b.31722.

[24] Q. Lin, Z. Xu, X. Lan, Y. Ni, C. Lu, The reactivity of nano silica with calcium hydroxide, J. Biomed. Mater. Res. - Part B Appl. Biomater. 99 B (2011) 239–246. Doi: 10.1002/jbm.b.31891.

[25] V. Daniele, G. Taglieri, A. Gregori, Synthesis of Ca(OH)2 Nanoparticles Aqueous Suspensions and Interaction with Silica Fume, Adv. Mater. Res. 629 (2013) 482–487, https://doi.org/10.4028/www.scientific.net/AMR.629.482.

[26] D. Chelazzi, G. Poggi, Y. Jaidar, N. Toccafondi, R. Giorgi, P. Baglioni, Hydroxide nanoparticles for cultural heritage: Consolidation and protection of wall paintings and carbonate materials, J. Colloid Interface Sci. 392 (2013) 42–49, https://doi.org/10.1016/j.jcis.2012.09.069.

[27] P. Baglioni, D. Chelazzi, R. Giorgi, G. Poggi, Colloid and materials science for the conservation of cultural heritage: Cleaning, consolidation, and deacidification, Langmuir 29 (2013) 5110–5122, https://doi.org/10.1021/la304456n.

[28] R. Camerini, D. Chelazzi, R. Giorgi, P. Baglioni, Hybrid nano-composites for the consolidation of earthen masonry, J. Colloid Interface Sci. 539 (2019), https://doi.org/10.1016/j.jcis.2018.12.082.

[29] L.P. Esteves, On the hydration of water-entrained cement-silica systems: Combined SEM, XRD and thermal analysis in cement pastes, Thermochim. Acta. 518 (2011) 27–35, https://doi.org/10.1016/j.tca.2011.02.003.

[30] F. Ridi, E. Fratini, S. Milani, P. Baglioni, Near-infrared spectroscopy investigation of the water confined in tricalcium silicate pastes, J. Phys. Chem. B. 110 (2006) 16326–16331, https://doi.org/10.1021/jp060026y.

[31] E. Fratini, F. Ridi, S.H. Chen, P. Baglioni, Hydration water and microstructure in calcium silicate and aluminate hydrates, J. Phys. Condens. Matter. 18 (2006) S2467–S2483, https://doi.org/10.1088/0953-8984/18/36/S18.

[32] F. Ridi, E. Fratini, P. Luciani, F. Winnefeld, P. Baglioni, Tricalcium silicate hydration reaction in the presence of comb-shaped superplasticizers: Boundary nucleation and growth model applied to polymer-modified pastes, J. Phys. Chem. C. 115 (2012) 10887–10895, https://doi.org/10.1021/jp209156n.

[33] W.S. Chiang, E. Fratini, F. Ridi, S.H. Lim, Y.Q. Yeh, P. Baglioni, S.M. Choi, U.S. Jeng, S.H. Chen, Microstructural changes of globules in calcium-silicate-hydrate gels with and without additives determined by small-angle neutron and X-ray scattering, J. Colloid Interface Sci. 398 (2013) 67–73, https://doi.org/10.1016/j.jcis.2013.01.065.

[34] E. Pustovgar, R.P. Sangodkar, A.S. Andreev, M. Palacios, B.F. Chmelka, R.J. Flatt, J.-B. d'Espinose de Lacaillerie, Understanding silicate hydration from quantitative analyses of hydrating tricalcium silicates, Nat. Commun. 7 (2016) 10952, https://doi.org/10.1038/ncomms10952.

[35] H.-C. Loh, H.-J. Kim, F.-J. Ulm, A. Masic, Time-Space-Resolved Chemical Deconvolution of Cementitious Colloidal Systems Using Raman Spectroscopy, Langmuir 37 (2021) 7019–7031, https://doi.org/10.1021/acs.langmuir.1c00609.

[36] F. Ridi, L. Dei, E. Fratini, S.H. Chen, P. Baglioni, Hydration kinetics of tri-calcium silicate in the presence of superplasticizers, J. Phys. Chem. B. 107 (2003) 1056–1061, https://doi.org/10.1021/jp027346b.

[37] F. Ridi, E. Fratini, F. Mannelli, P. Baglioni, Hydration process of cement in the presence of a cellulosic additive. A calorimetric investigation, J. Phys. Chem. B. 109 (2005) 14727–14734, https://doi.org/10.1021/jp050237n.

[38] H. Li, W.S. Chiang, E. Fratini, F. Ridi, F. Bausi, P. Baglioni, M. Tyagi, S.H. Chen, Dynamic crossover in hydration water of curing cement paste: The effect of superplasticizer, J. Phys. Condens. Matter. 24 (2012) 1–7, https://doi.org/10.1088/0953-8984/24/6/064108.

[39] S. Del Buffa, E. Fratini, F. Ridi, A. Faraone, P. Baglioni, State of Water in Hydrating Tricalcium Silicate Pastes: The Effect of a Cellulose Ether, J. Phys. Chem. C. 120 (2016) 7612–7620, https://doi.org/10.1021/acs.jpcc.6b00691.

[40] J.J. Thomas, A new approach to modeling the nucleation and growth kinetics of tricalcium silicate hydration, J. Am. Ceram. Soc. 90 (2007) 3282–3288, https://doi.org/10.1111/j.1551-2916.2007.01858.x.

[41] R. Camerini, G. Poggi, D. Chelazzi, F. Ridi, R. Giorgi, P. Baglioni, The carbonation kinetics of calcium hydroxide nanoparticles: A Boundary Nucleation and Growth description, J. Colloid Interface Sci. 547 (2019) 370–381, https://doi.org/10.1016/j.jcis.2019.03.089.

[42] G. Poggi, N. Toccafondi, L.N. Melita, J.C. Knowles, L. Bozec, R. Giorgi, P. Baglioni, Calcium hydroxide nanoparticles for the conservation of cultural heritage: New formulations for the deacidification of cellulose-based artifacts, Appl. Phys. A Mater. Sci. Process. 114 (2014) 685–693, https://doi.org/10.1007/s00339-013-8172-7.

[43] G. Poggi, N. Toccafondi, D. Chelazzi, P. Canton, R. Giorgi, P. Baglioni, Calcium hydroxide nanoparticles from solvothermal reaction for the deacidification of degraded waterlogged wood, J. Colloid Interface Sci. 473 (2016) 1–8, https://doi.org/10.1016/j.jcis.2016.03.038.

[44] J.W. Cahn, The kinetics of grain boundary nucleated reactions, Acta Metall. 4 (1956) 449–459, https://doi.org/10.1016/0001-6160(56)90041-4.

[45] F. Ridi, E. Fratini, P. Luciani, F. Winnefeld, P. Baglioni, Hydration kinetics of tricalcium silicate by calorimetric methods, J. Colloid Interface Sci. 364 (2011) 118–124, https://doi.org/10.1016/j.jcis.2011.08.010.

[46] V.K. Peterson, A.E. Whitten, Hydration processes in tricalcium silicate: Application of the boundary nucleation model to quasielastic neutron scattering data, J. Phys. Chem. C. 113 (2009) 2347–2351, https://doi.org/10.1021/jp807209w.

[47] J.J. Thomas, A.J. Allen, H.M. Jennings, Hydration kinetics and microstructure development of normal and CaCl 2-accelerated tricalcium silicate pastes, J. Phys. Chem. C. 113 (2009) 4327–4334, https://doi.org/10.1021/jp907078u.

[48] J.W. Christian, The theory of transformations in metals and alloys, 3rd edition, Pergamon Press, Oxford, 2002, 2002. Doi: http://dx.doi.org/10.1016/B978-008044019-4/50015-5.

[49] T.A. Ring, Fundamentals of Ceramic Powder Processing and Synthesis, Academic Press, San Diego, 1997.

[50] S. Björkegren, L. Nordstierna, A. Sundblom, A. Palmqvist, Clouding observed for surface active, mPEG-grafted silica nanoparticles, RSC Adv. 9 (2019) 13297–13303, https://doi.org/10.1039/C9RA00361D.

[51] K. Baltakys, R. Jauberthie, R. Siauciunas, R. Kaminskas, Influence of modification of SiO2 on the formation of calcium silicate hydrate, Mater. Sci. 25 (2007) 663–670.

[52] E. Carretti, D. Chelazzi, G. Rocchigiani, P. Baglioni, G. Poggi, L. Dei, Interactions between Nanostructured Calcium Hydroxide and Acrylate Copolymers: Implications in Cultural Heritage Conservation, Langmuir 29 (2013) 9881–9890, https://doi.org/10.1021/la401883g.

[53] N. Vagenas, Quantitative analysis of synthetic calcium carbonate polymorphs using FT-IR spectroscopy, Talanta 59 (2003) 831–836, https://doi.org/10.1016/S0039-9140(02)00638-0.

[54] L. Andersen, Flemming A. Brečević, Infrared Spectra of Amorphous and Crystalline Calcium Carbonate, Acta Chem. Scand. 45 (1991) 1018–1024, https://doi.org/10.3891/acta.chem.scand.45-1018.

[55] S. Gunasekaran, G. Anbalagan, S. Pandi, Raman and infrared spectra of carbonates of calcite structure, J. Raman Spectrosc. 37 (2006) 892–899, https://doi.org/10.1002/jrs.1518.

[56] I. Wilińska, B. Pacewska, Influence of selected activating methods on hydration processes of mixtures containing high and very high amount of fly ash, J. Therm. Anal. Calorim. 133 (2018) 823–843, https://doi.org/10.1007/s10973-017-6915-y.

[57] C. Narattha, A. Chaipanich, Effect of curing time on the hydration and material properties of cold-bonded high-calcium fly ash–Portland cement lightweight aggregate, J. Therm. Anal. Calorim. (2020), https://doi.org/10.1007/s10973-020-09730-8.

[58] F. Ridi, E. Fratini, R. Alfani, P. Baglioni, Influence of acrylic superplasticizer and cellulose-ether on the kinetics of tricalcium silicate hydration reaction, J. Colloid Interface Sci. 395 (2013) 68–74, https://doi.org/10.1016/j.jcis.2012.12.048.

[59] A. Khawam, D.R. Flanagan, Solid-state kinetic models: Basics and mathematical fundamentals, J. Phys. Chem. B. 110 (2006) 17315–17328, https://doi.org/10.1021/jp062746a.

[60] P. Khuman, W.B.K. Singh, S.D. Devi, H. Naorem, Viscosity-Temperature Behavior of Hydroxypropyl Cellulose Solution in Presence of an Electrolyte

or a Surfactant: A Convenient Method to Determine the Cloud Point of Polymer Solutions, J. Macromol. Sci. Part A. 51 (2014) 924–930, https://doi.org/10.1080/10601325.2014.953377.

[61] M. Alesiani, S. Capuani, R. Giorgi, B. Maraviglia, I. Pirazzoli, F. Ridi, P. Baglioni, Influence of Cellulosic Additives on Tricalcium Silicate Hydration: Nuclear Magnetic Resonance Relaxation Time Analysis, J. Phys. Chem. B. 108 (2004) 4869–4874, https://doi.org/10.1021/jp037876n.

[62] M. Tonelli, F. Martini, A. Milanesi, L. Calucci, M. Geppi, S. Borsacchi, F. Ridi, Effect of phosphate additives on the hydration process of magnesium silicate cements, J. Therm. Anal. Calorim. 138 (2019) 3311–3321, https://doi.org/10.1007/s10973-019-08847-9.

[63] S.A. Walling, J.L. Provis, Magnesia-Based Cements: A Journey of 150 Years, and Cements for the Future?, Chem Rev. 116 (2016) 4170–4204, https://doi.org/10.1021/acs.chemrev.5b00463.